Journal of Power Sources 215 (2012) 152–159

Contents lists available at SciVerse ScienceDirect

Journal of Power Sources

journal homepage: www.elsevier.com/locate/jpowsour

Effects of annealing and stoichiometry to (Nd, Mg)(Ni, Al)$_{3.5}$ metal hydride alloys

K. Young*, T. Ouchi, B. Huang

Ovonic Battery Company, 2983 Waterview Drive, Rochester Hills, MI 48309, USA

HIGHLIGHTS

- The influences of stoichiometry and annealing to Nd-A2B7 alloys were studied.
- Secondary phases are critical as catalyst for hydrogen storage.
- Annealing improves capacity and high-rate dischargeability.
- Annealed AB3.5 has the best electrochemical properties.

ARTICLE INFO

Article history:
Received 30 March 2012
Received in revised form
1 May 2012
Accepted 3 May 2012
Available online 14 May 2012

Keywords:
Hydrogen storage materials
Hydrogen absorption
Metal hydride electrode
Electrochemical reactions

ABSTRACT

The structures, gaseous phase hydrogen storage, and electrochemical properties of a series of $(Nd_{0.83}Mg_{0.16}Zr_{0.01})(Ni_{0.953}Al_{0.046}Co_{0.001})_{\alpha}$ alloys, where α = 3.3, 3.4, 3.5, 3.6, and 3.7, before and after annealing (900 °C and 5 h in argon) were studied. Besides the main Nd_2Ni_7 phase, other secondary phases, such as $MgNdNi_4$, $NdNi_5$, $NdNi_3$, NdNi, and $CeNi_3$, were present in most of the samples and influenced the hydrogen storage properties. After annealing, several changes happened: the stoichiometry of the main Nd_2Ni_7 phase remained constant at B/A = 3.3 and its abundance increased; the abundances of the major secondary phases decreased but were not totally eliminated (which helped preserve the catalytic effects); both the gaseous phase hydrogen storage and electrochemical capacity increased; the high-rate dischargeability decreased slightly; and the activation became more difficult. A stoichiometry of AB3.5 showed the best compromise among electrochemical capacity, high-rate dischargeability, and ease of activation.

1. Introduction

Rare earth (RE) magnesium-based AB_3- or A_2B_7-types of metal hydride (MH) alloys are promising candidates to replace the currently used AB_5 MH alloys as the negative electrodes in nickel/metal hydride (Ni/MH) batteries due to their high capacities and good high-rate dischargeability (HRD) [1]. The structures of AB_3- ($CeNi_3$ or $PuNi_3$) and A_2B_7-types (Ce_2Ni_7 or Gd_2Ni_7) are similar [2], being composed of alternating A_2B_4 (Laves-type) and AB_5 construction blocks [3,4]. Other similar A_2B_4/AB_5 mixed structures, such as Pr_5Co_{19} and Ce_5Co_{19} [5–13], were also proposed as MH alloys. While most of the RE-Mg–Ni MH alloys were based on La-only cases [4,14–23], other RE metals in misch-metal form were also considered [24–26]. Nd is an RE element with lower chemical activity compared to La and can be used to increase the oxidation resistance and extend the cycle life of the RE–Mg–Ni MH alloys. Mixed (La, Nd)–Mg–Ni alloys were studied, and a small amount of Nd (10% of A-site) was shown to increase both the surface exchange current and bulk diffusion and thus improve the HRD [27,28], cycle stability [29,30], and discharge capacity [31]. Another study in low-Co (La, Nd)–Mg–Ni alloys showed that 50% of Nd in A-site gave the best combination of capacity, HRD, and cycle stability [32].

Studies on Nd as the only RE element in RE–Mg–Ni MH alloys have been conducted before. A series of $Nd_{0.75}Mg_{0.25}(Ni_{0.8}Co_{0.2})_{\alpha}$ alloys, where α = 3.5 [33], 3.8 [34], and 4.5 [34], was studied. The sample with $AB_{3.5}$ stoichiometry showed the highest electrochemical capacity and HRD. While comparing the different preparation methods of the same $Nd_{0.75}Mg_{0.25}(Ni_{0.8}Co_{0.2})_{3.5}$ alloy, the thermal annealing at 900 °C yielded the highest discharge capacity [33]; the magnetic annealing at 650 °C showed the best HRD [35]; and the quick quench by melt-spinning promoted the most stable cycle performance [36]. In a study of annealed $Nd_{0.88}Mg_{0.12}Ni_{3.10+x}Al_{0.20}$ (x = 0.0, 0.1, 0.2, 0.3) alloy, a stoichiometry of $AB_{3.5}$ showed the best charge retention and cycle stability [37]. Although the electrochemical properties of

* Corresponding author. Tel.: +1 248 293 7000; fax: +1 248 299 4520.
E-mail address: kwoyoung@yahoo.com (K. Young).

0378-7753/$ – see front matter © 2012 Elsevier B.V. All rights reserved.
doi:10.1016/j.jpowsour.2012.05.006

Mg–Nd–Ni based A_2B_7 were studied before, the contributions from annealing and secondary phases were not discussed. Therefore, both the annealing and stoichiometry of a series of Nd-based A_2B_7 alloys are examined in detail and reported in this study.

2. Experimental setup

Ingots were prepared in a 2-kg induction furnace from raw materials in elemental form (except for Mg, where $MgNi_2$ was used to suppress the evaporation of Mg) under 1 atm of helium. Extra amount of Mg was added to compensate the losses during melting and annealing. The ingot was annealed at 900 °C for 5 h in 1 atm of argon. The annealing conditions were optimized by the electrochemical properties with the same methodology used in the annealing experiment on the mish-metal based A_2B_7 alloys reported previously [38]. The chemical composition of each sample was examined by a Varian *Liberty* 100 inductively-coupled plasma (ICP) system. A Philips *X'Pert Pro* x-ray diffractometer (XRD) was used to study the microstructure, and a JOEL-*JSM6320F* scanning electron microscopy (SEM) with energy dispersive spectroscopy (EDS) capability was used to study the phase distribution and composition. PCT characteristics for each sample were measured using a Suzuki-Shokan multi-channel PCT system. In the PCT analysis, each sample was first activated by a 2-h thermal cycle between 300 °C and room temperature at 25 atm H_2 pressure. The PCT isotherms at 30, 45, and 60 °C were then measured.

For the electrochemical study, the ingot was first ground and then passed through a 200-mesh sieve. The sieved powder was then compacted onto an expanded nickel metal substrate by a 10-ton press to form a test electrode (about 1 cm^2 in area and 0.2 mm thick) without using any binder. Discharge capacities of these small-sized electrodes were measured in a flooded-cell configuration using a partially pre-charged $Ni(OH)_2$ pasted electrode as the positive electrode and a 6 M KOH solution as the electrolyte. The system was charged at a current density of 100 mA g^{-1} for 5 h and then discharged at a current density of 100 mA g^{-1} until a cut-off voltage of −0.9 V was reached. The system was then discharged at a current density of 24 mA g^{-1} until a cut-off voltage of −0.9 V was reached and finally discharged at a current density of 8 mA g^{-1} until a cut-off voltage of −0.9 V was reached. Linear polarization was performed by scanning the potential from −20 to +20 mV of the open circuit voltage at a rate of 0.1 mV s^{-1}. For the potentiostatic discharge experiment, electrode in a fully charged state was polarized +0.6 V vs. the open circuit voltage for 7200 s.

Table 1
Design compositions and ICP results in at.%.

Alloy		Nd	Zr	Mg	Ni	Co	Al	Fe	B/A
AB3.3	Design	19.3	0.2	3.7	73.1	0.1	3.5	0.0	3.30
	ICP as-cast	19.4	0.2	3.8	73.1	0.1	3.4	0.1	3.28
	ICP annealed	19.1	0.2	3.8	73.2	0.1	3.4	0.1	3.32
AB3.4	Design	18.9	0.2	3.6	73.7	0.1	3.5	0.0	3.41
	ICP as-cast	19.0	0.2	3.4	73.7	0.1	3.5	0.1	3.42
	ICP annealed	18.8	0.2	3.3	73.9	0.1	3.6	0.1	3.48
AB3.5	Design	18.4	0.2	3.6	74.1	0.1	3.5	0.0	3.50
	ICP as-cast	18.5	0.2	3.5	74.1	0.1	3.5	0.1	3.50
	ICP annealed	18.2	0.2	3.6	74.3	0.1	3.6	0.1	3.55
AB3.6	Design	18.0	0.2	3.5	74.6	0.1	3.5	0.0	3.60
	ICP as-cast	18.3	0.2	3.4	74.3	0.1	3.5	0.1	3.56
	ICP annealed	18.0	0.2	3.6	74.6	0.1	3.4	0.1	3.59
AB3.7	Design	17.7	0.2	3.4	75.0	0.1	3.6	0.0	3.70
	ICP as-cast	17.6	0.2	3.5	75.0	0.1	3.5	0.1	3.70
	ICP annealed	17.8	0.2	3.4	74.9	0.1	3.5	0.1	3.67

3. Results and discussion

Five alloys (ABα) with design formula $(Nd_{0.83}Mg_{0.16}Zr_{0.01})(Ni_{0.953}Al_{0.046}Co_{0.001})_\alpha$, where α = 3.3, 3.4, 3.5, 3.6, and 3.7, were prepared. ABαA denotes alloy after annealing. These alloys are similar to those reported in Ref. 37 with the addition of a very small amount of Zr to enhance the cycle life [39] and Co to facilitate activation [40]. The ICP results from ingots before and after annealing in atomic percentage are compared in Table 1, which are very close to the designed compositions shown in the same table

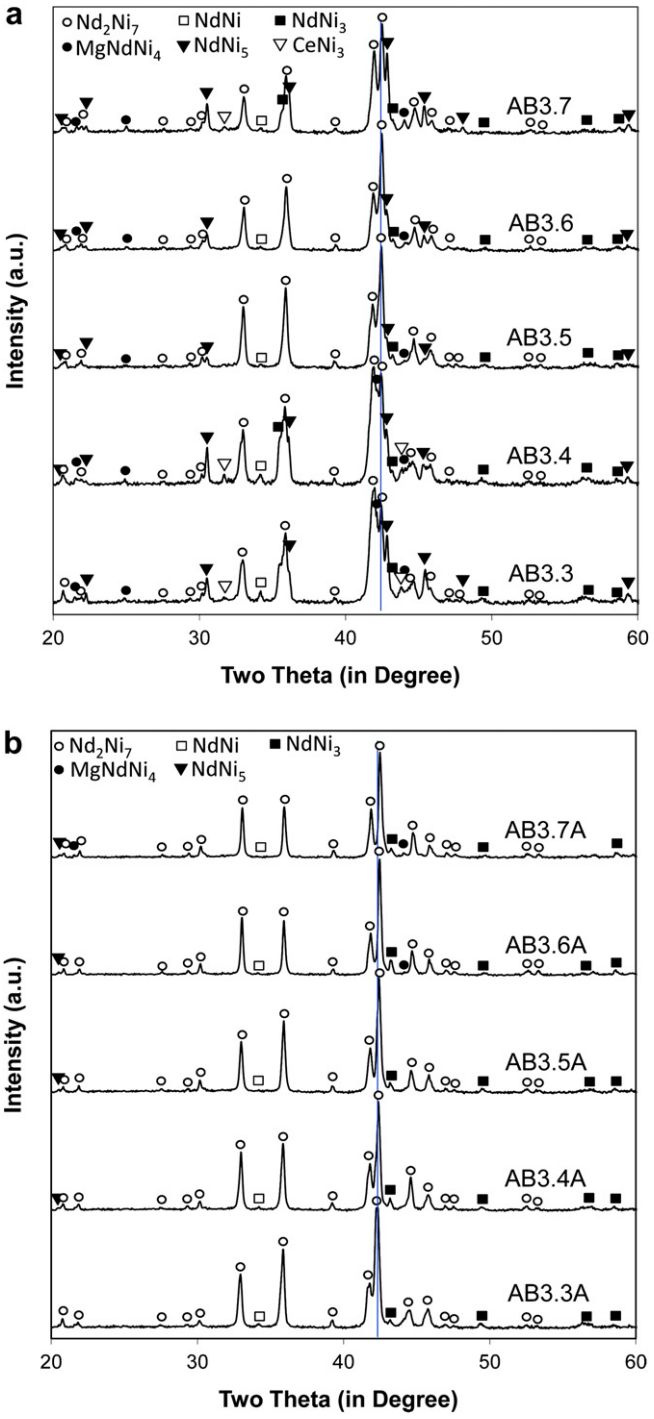

Fig. 1. XRD patterns using Cu-K_α as the radiation source for as-cast (a) and annealed (b) Samples.

except for a small amount of Fe pick-up from the steel mold. The final B/A ratio after annealing for alloys AB3.3, AB3.4, AB3.5, AB3.6 and AB3.7 are 3.32, 3.48, 3.55, 3.59, and 3.67, respectively.

3.1. XRD analysis

The XRD patterns of the five alloys before and after annealing are shown in Fig. 1a and b, respectively. All patterns are dominated by a Nd_2Ni_7 structure. $NdNi_5$ and $MgNdNi_4$ are the main secondary phases, and their abundances reduce after annealing. Lattice constants a and c from the main Nd_2Ni_7 for each alloy are listed in Table 2 together with the c/a ratio and unit cell volume. In both the as-cast and annealed series, lattice constant a remains about the same while the lattice constant c reduces as the B/A ratio increases, which causes the decreases in both c/a ratio and unit cell volume. The c/a ratio is important for the prediction of the pulverization rate of AB_2 and AB_5 alloys. Due to the different directions for the proton to transport in AB_2 (along c-axis) and AB_5 (along a–b plane) MH alloys [41,42], the former prefers a smaller while the later prefers a larger c/a ratio to decrease the pulverization during hydriding/dehydriding cycles [43,44]. The Nd_2Ni_7 structure is the stacking of AB_5 and 2 × AB_2 units, and the preferential sites for deuterium are all in the AB_2 slabs according to the XRD study [45,46]. Consequently, the protons will likely hop along the a–b plane as in the case of AB_5 MH alloy. A larger c/a ratio may contribute to a shorter distance for the protons to hop. However, more elongation along the c-axis during the hydride from a smaller a lattice constant may promote an easier pulverization. Therefore, the effect of the decrease in c/a ratio with the increase in B/A ratio on the cycle stability is unclear and requires further investigation. Finally, the reductions in unit cell volume in both series as the B/A ratio increases are plotted in Fig. 2. After annealing, the unit cell volume increases at every stoichiometry, which corresponds to a more stable hydride with stronger metal-bond strength [44,47].

The phase abundances analyzed by Jade 9 software are listed in Table 2. Before annealing, $MgNdNi_4$ and $NdNi_5$ are the main secondary phases with Nd, NdNi, $NdNi_3$, and $CeNi_3$ as the minor secondary phases. Both $MgNdNi_4$ [48–53] and $NdNi_5$ [54–56] are MH alloys studied previously. In both the as-cast and annealed series, the abundance of the main Nd_2Ni_7 phase decreases with increases in phase abundances of $NdNi_5$ and $MgNdNi_4$ as the design B/A ratio increases except for AB3.3. $CeNi_3$ is a different crystal structure from the $NdNi_3$ ($PuNi_3$ structure) [2]. The abundances of the minor secondary phases reduce with the increase in B/A ratio. After annealing, while the abundances of the all secondary phases reduce and the abundance of the main Nd_2Ni_7 phase increases. The annealing condition was optimized by the electrochemical performance, and the synergetic effect from the secondary phases was intentionally preserved for the same reason as in AB_2 alloy development [57,58]. The effects of this increase in Nd_2Ni_7 phase abundance on the gaseous and electrochemical hydrogen storages will be discussed in later sections.

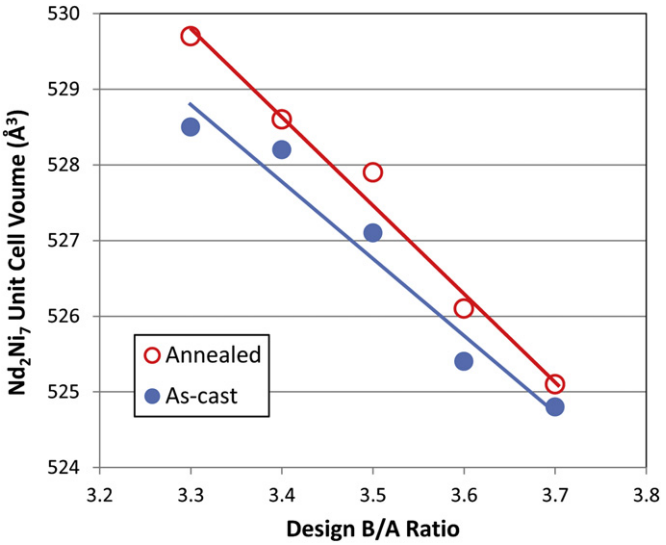

Fig. 2. Unit cell volumes of the Nd_2Ni_7 main phase as functions of design B/A ratio.

3.2. SEM/EDS analysis

The microstructures for alloys before and after annealing were studied by SEM, and the backscattering electron images (BEI) are presented in Fig. 3a–e, and f–j, respectively. Samples were mounted and polished on epoxy blocks, rinsed and dried before entering the SEM chamber. The compositions in several areas (identified numerically in the micrographs) were studied by EDS, and some of the results are listed in Table 3. In all micrographs, phases with the brightest (area #1) and darkest (area #7) contrasts are from Nd and ZrO_2, respectively. Besides the main Nd_2Ni_7 phase, a phase with a brighter contrast and a typical B/A ratio between 2.7 and 2.9 is found in all as-cast alloys (Fig. 3a-2, b-2, b-3, c-2, c-3, d-3, e-2, e-3) and AB3.3A (Figs. 3f-4) and AB3.4A (Fig. 3g-4). This stoichiometry is very close to that of $NdNi_3$ (B/A ratio = 3.0), which has a very similar structure to Nd_2Ni_7 [2]. In a few samples (AB3.6, AB3.3A, AB3.4A, and AB3.5A), the phase with a brighter contrast than $NdNi_3$ and a B/A ratio of about 1.0 is attributed to the NdNi phase (Fig. 3d-2, f-2). Moreover, a phase with a slightly darker contrast than the main Nd_2Ni_7 phase can be found in all samples (area #6 for AB3.3A, 3.4A, and 3.7A and area #5 for the rest of alloys). The Mg-content in this particular phase is the highest. With a stoichiometry of exactly 2.0, this phase is assigned as the $MgNdNi_4$ phase. The phase with the second darkest contrast (area #6) in the as-cast alloys and a B/A ratio of 4.6 is assigned as

Table 2
Nd_2Ni_7 lattice constants and ratios, unit cell volumes, and phase abundances of alloys from XRD analysis.

Alloy	a (Å)	c (Å)	c/a	Unit cell volume (Å^3)	$NdNi_5$ %	Nd_2Ni_7 %	$NdNi_3$ %	$MgNdNi_4$ %	NdNi %	$CeNi_3$ %
AB3.3	4.999	24.423	4.886	528.5	4.8	87.2	2.1	2.8	2.1	1.0
AB3.4	5.003	24.373	4.872	528.2	2.8	88.8	2.7	3.6	1.3	0.8
AB3.5	5.000	24.352	4.871	527.1	3.2	86.2	2.5	7.6	0.3	0.2
AB3.6	4.994	24.325	4.871	525.4	3.6	85.4	2.2	8.4	0.4	0.0
AB3.7	4.992	24.318	4.871	524.8	5.8	79.6	3.6	10.2	0.4	0.4
AB3.3A	5.004	24.433	4.883	529.7	0.2	97.0	2.0	0.4	0.4	0.0
AB3.4A	5.006	24.360	4.866	528.6	0.5	96.5	2.1	0.6	0.3	0.0
AB3.5A	5.001	24.372	4.873	527.9	0.4	96.5	1.8	1.2	0.1	0.0
AB3.6A	4.999	24.314	4.864	526.1	0.8	95.0	3.2	0.8	0.2	0.0
AB3.7A	4.997	24.284	4.860	525.1	0.7	94.9	1.7	2.6	0.1	0.0

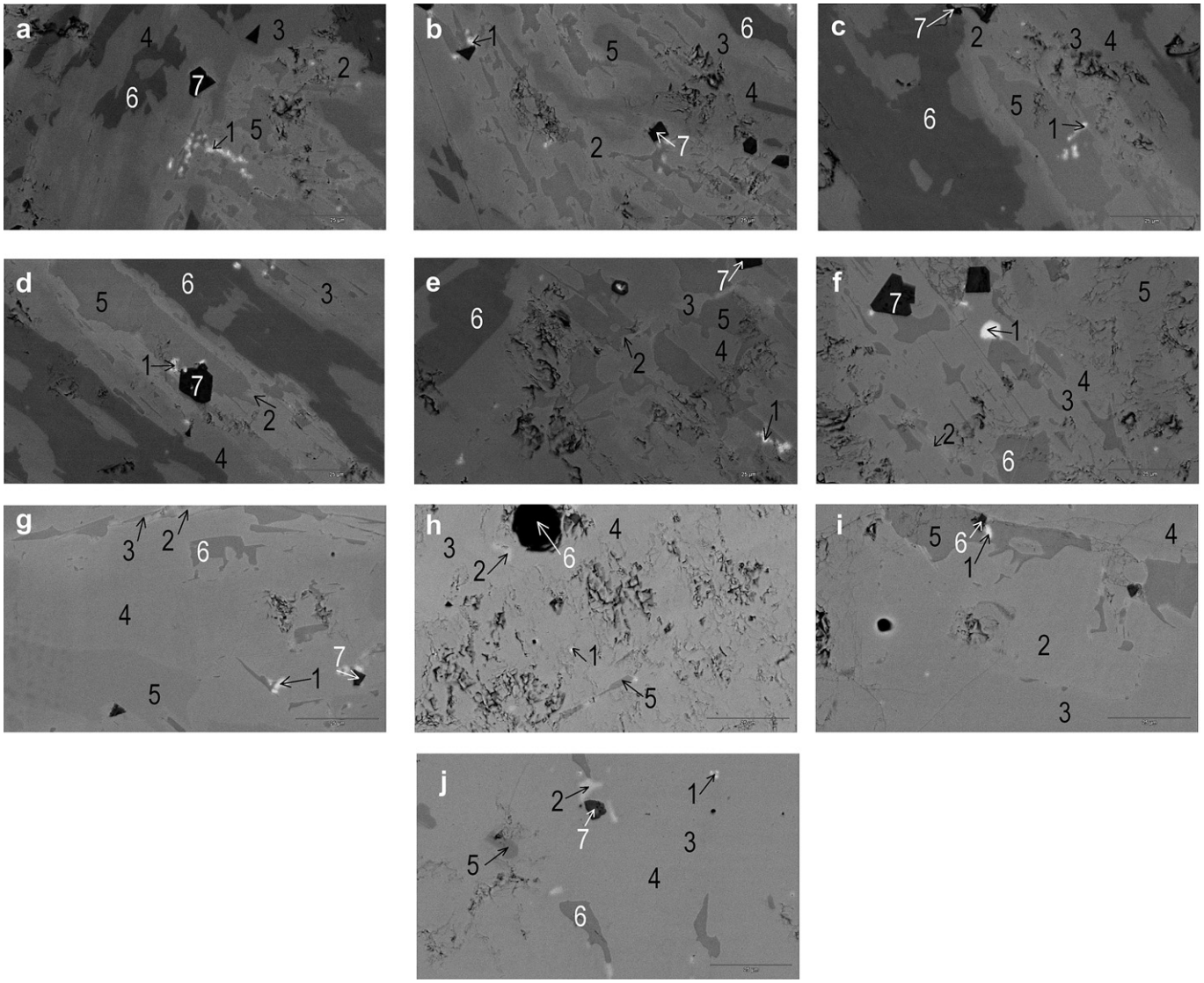

Fig. 3. SEM backscattering images for alloys AB3.3 (a), AB3.4 (b), AB3.5 (c), AB3.6 (d), AB3.7 (e), AB3.3A (f), AB3.4A (g), AB3.5A (h), AB3.6A (i), and AB3.7A (j). The chemical compositions of some areas indicated by Arabic numerals were studied by EDS, and the results are summarized in Table 3.

the $NdNi_5$ phase. This phase is absent in all the micrographs of the annealed ingots. From the Nd–Ni phase diagram [59], the solidification sequence can be estimated as first $NdNi_5$, followed by Nd_2Ni_7, $NdNi_3$, $NdNi_2$ ($MgNdNi_4$), and finally to NdNi. As a consequence, the $NdNi_5$ that solidified first and the $MgNdNi_4$ that solidified later do not share any common boundary as shown in the micrographs. According to the EDS analysis, the solubility of Mg in various phases is in the order of $MgNdNi_4 > NdNi_3 > Nd_2Ni_7 > NdNi > NdNi_5$, which is almost opposite to the cooling sequence. This indicates that during solidification, Mg is passed to the next solidified phase sequentially. The solubility of Al in the $MgNdNi_4$ is the less than its solubility in all other phases. Comparing the overall micrographs from the as-cast and annealed ingots, the main secondary phases ($NdNi_5$ and $MgNdNi_4$) either become smaller or disappear while the main Nd_2Ni_7 phase expands after annealing. The amounts of the minor secondary phases, such as NdNi and $NdNi_3$, remain about the same after annealing.

As the design B/A ratio increases from 3.3 to 3.7, the stoichiometries of the main Nd_2Ni_7 phases (**bold** in Table 3) in the as-cast series decrease from 3.7 to 3.3 and those in the annealed series remain at 3.3. The deviation in the as-cast samples is due to the increase in abundance of $NdNi_5$ phase (higher Ni-content) with the increase in B/A ratio. After annealing, the phase abundance of $NdNi_5$ phase decreases and is just enough to maintain the stoichiometry of the main phase at 3.3.

3.3. Gaseous phase study

The gaseous phase hydrogen storage properties of the alloys were studied by PCT measured at 30, 45, and 60 °C. The resulting absorption and desorption isotherms measured at 30 °C for the as-cast and annealed series are shown in Fig. 4a and b, respectively. The information obtained from the PCT study is summarized in Table 4. The maximum hydrogen storage capacity measured at 30 °C for both the as-cast and annealed series first increases and then stabilizes as the B/A ratio increases. The reversible hydrogen storage capacity measured at 30 °C increases with the increase in B/A ratio in both the as-cast and annealed series. The increases in both storage capacities can be attributed to the increase in abundance of the $NdNi_5$ phase, which is a catalytic phase with a weaker metal-hydrogen bond. Annealing improves both the maximum and

Table 3
Summary of some EDS results. Data from annealed samples are similar and thus only those from AB3.3A are shown here. Areas #1 and #7 are the Nd and ZrO_2 phases, respectively. The main Nd_2Ni_7 phases are in **bold**.

Alloy	Location	Nd	Zr	Mg	Ni	Al	B/A	Phase
AB3.3	Fig. 3a-2	22.5	0.1	3.9	68.9	4.6	2.8	AB_3
	Fig. 3a-3	20.0	0.1	2.8	73.4	3.6	3.4	Nd_2Ni_7
	Fig. 3a–4	**19.0**	**0.1**	**2.4**	**74.5**	**4.0**	**3.7**	**Nd_2Ni_7**
	Fig. 3a-5	22.2	0.1	10.8	65.9	1.0	2.0	$MgNdNi_4$
	Fig. 3a-6	17.1	0.0	0.7	77.4	4.8	4.6	$NdNi_5$
AB3.4	Fig. 3b-2	21.5	0.2	4.2	70.0	4.0	2.9	AB_3
	Fig. 3b-3	21.1	0.0	5.1	70.6	3.1	2.8	AB_3
	Fig. 3b-4	**19.0**	**0.2**	**2.3**	**74.8**	**3.7**	**3.7**	**Nd_2Ni_7**
	Fig. 3b-5	22.5	0.0	10.9	65.6	1.0	2.0	$MgNdNi_4$
	Fig. 3b-6	17.2	0.1	0.5	77.9	4.3	4.6	$NdNi_5$
AB3.5	Fig. 3c-2	22.0	0.0	4.9	69.7	3.5	2.7	AB_3
	Fig. 3c-3	20.8	0.2	4.9	70.8	3.4	2.9	AB_3
	Fig. 3c-4	**19.0**	**0.2**	**3.1**	**74.6**	**3.0**	**3.5**	**Nd_2Ni_7**
	Fig. 3c-5	22.1	0.0	10.9	65.4	1.5	2.0	$MgNdNi_4$
	Fig. 3c-6	17.3	0.1	0.4	77.4	4.8	4.6	$NdNi_5$
AB3.6	Fig. 3d-2	48.6	0.2	1.0	50.3	0.0	1.0	NdNi
	Fig. 3d-3	22.4	0.1	4.2	69.0	4.2	2.7	AB_3
	Fig. 3d-4	**19.5**	**0.1**	**3.4**	**73.0**	**3.4**	**3.3**	**Nd_2Ni_7**
	Fig. 3d-5	21.6	0.0	11.3	66.1	1.0	2.0	$MgNdNi_4$
	Fig. 3d-6	17.3	0.1	0.4	78.6	3.6	4.6	$NdNi_5$
AB3.7	Fig. 3e-2	21.7	0.1	4.0	70.4	3.9	2.9	AB_3
	Fig. 3e-3	21.4	0.1	4.3	70.1	4.1	2.9	AB_3
	Fig. 3e-4	**19.2**	**0.1**	**4.2**	**73.1**	**3.3**	**3.3**	**Nd_2Ni_7**
	Fig. 33-5	19.8	0.1	13.1	66.1	0.9	2.0	$MgNdNi_4$
	Fig. 3e-6	17.1	0.1	0.6	78.8	3.4	4.6	$NdNi_5$
AB3.3A	Fig. 3f-2	44.6	0.2	1.2	53.4	0.6	1.2	NdNi
	Fig. 3f-3	22.4	0.1	4.0	69.3	4.2	2.8	AB_3
	Fig. 3f-4	22.4	0.2	4.4	69.5	3.4	2.7	AB_3
	Fig. 3**5**	**20.1**	**0.1**	**3.0**	**72.5**	**4.2**	**3.3**	**Nd_2Ni_7**
	Fig. 3f-6	21.6	0.0	11.9	65.7	0.8	2.0	$MgNdNi_4$

reversible hydrogen storage capacities due to the reduction in abundance of the $MgNdNi_4$ phase, which has a lower hydrogen storage capacity [51]. The equilibrium plateau pressure, defined as the mid-point of the desorption isotherm, decreases and then increases in the as-cast series and increases monotonically in the annealed series with the increase in B/A ratio. Both the capacities and pressures measured by PCT are different from the prediction of the XRD analysis that show a shrinking unit cell volume of the main Nd_2Ni_7 phase with increasing B/A ratio in both the as-cast and annealed series (due to the presence of the secondary phases acting as catalysts for hydrogen storage). The slope factor (SF) is defined as the ratio of the storage capacity between 0.01 and 5 MPa to the reversible capacity. The SF of each alloy is listed in Table 4 and can be used to predict the degree of disorder in the alloy [60,61]. While the trend of SF evolution in the as-cast series is not clear, the annealed samples show improvement in SF with the increase in B/A ratio. Annealing for the multi-phase A_2B_7 alloys does not necessarily improve the SF, which is different from the case in AB_5 with a single $CaCu_5$ crystal structure [62]. The hysteresis of the PCT isotherm of each alloy, listed in Table 4, is defined as $\ln(P_a/P_d)$, where P_a and P_d are the absorption and desorption equilibrium pressures at the mid-point, respectively. The hysteresis can be used to predict the pulverization rate of the alloy during cycling [63]. Alloys with larger hystereses have higher pulverization rates during hydriding/dehydriding cycles. As the B/A ratio increases, the hysteresis in the as-cast series decreases while that in the annealed series remains about the same. The annealing reduces the hysteresis in general except for the AB3.7 alloy.

Desorption equilibrium pressures at mid-point measured at 30, 45, and 60 °C were used to calculate the changes in enthalpy (ΔH) and entropy (ΔS) by the equation

$$\Delta G = \Delta H - T\Delta S = RT\ln P \quad (1)$$

where R is the ideal gas constant and T is the absolute temperature. The results of these calculations are listed in Table 4. All the ΔH values are between −36 and −41 kJ mol^{-1} H_2, which are comparable to the commercially available AB_5 and AB_2 MH alloys [64,65]. ΔH of the as-cast series decreases with the increase in B/A ratio and

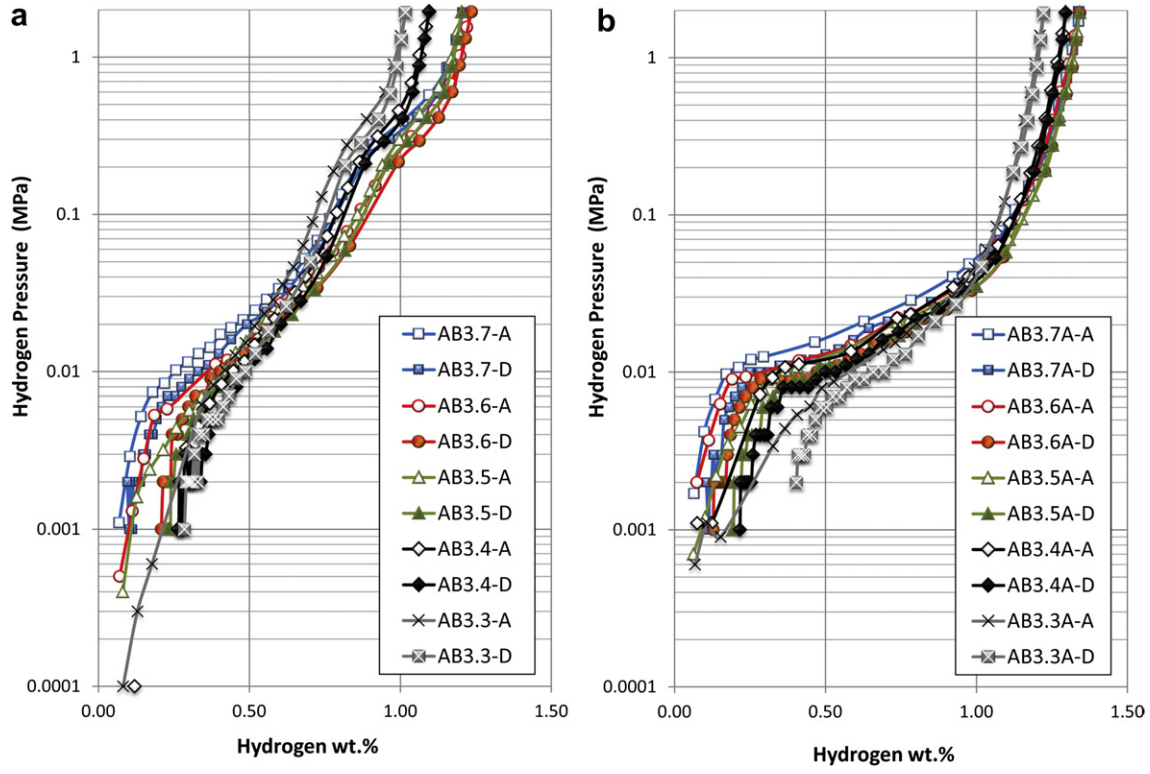

Fig. 4. PCT isotherms of as-cast (a) and annealed (b) Samples measured at 30 °C. Open and solid symbols are for absorption and desorption curves, respectively.

Table 4
Summary of gaseous phase hydrogen storage properties of as-cast and annealed alloys.

Alloy	Max. H-storage at 30 °C (wt. %)	Rev. H-storage at 30 °C (wt. %)	Mid-point pressure at 30 °C Des. (MPa)	30 °C slope factor	30 °C hysteresis	$-\Delta H$ (kJ mol^{-1} H_2)	$-\Delta S$ (J K^{-1} mol^{-1} H_2)
AB3.3	1.11	0.82	0.050	0.56	0.58	36	114
AB3.4	1.10	0.82	0.034	0.66	0.21	36	111
AB3.5	1.20	0.97	0.033	0.54	0.22	38	116
AB3.6	1.23	1.04	0.033	0.88	0.26	39	118
AB3.7	1.21	1.11	0.041	0.68	0.08	39	121
AB3.3A	1.22	0.84	0.016	0.58	0.22	40	115
AB3.4A	1.30	1.10	0.018	0.65	0.19	40	118
AB3.5A	1.34	1.16	0.018	0.71	0.18	41	121
AB3.6A	1.34	1.22	0.019	0.76	0.18	40	119
AB3.7A	1.34	1.24	0.022	0.77	0.19	40	118

remains the same for the annealed series, which is in agreement with the stoichiometry of the main Nd_2Ni_7 phase as found in the SEM/EDS study. ΔH of the annealed sample is usually lower than that of the as-cast sample. The ΔS values are very similar and slightly larger than ΔS between the hydrogen gas and hydrogen in the solid (-125 J K^{-1} mol^{-1} H_2) [66]. This indicates that the β-phase (hydride) of the alloys under current study is close to but not in perfectly ordered structure, which reduces ΔS slightly. The deviation from a perfect hydride is more obvious with AB_2 alloys carrying higher degree of disorder, which show even larger ΔS [67,68].

3.4. Electrochemical measurement

The discharge capacity of each alloy was measured in a flooded-cell configuration against a partially pre-charged $Ni(OH)_2$ positive electrode. The purpose of the current setup is to measure the activation behavior and thus no binder or other metal was added. Consequently, the pressed electrode is not as durable as those with Ni or Cu powder added and is not intended for cycle life evaluation. No alkaline pretreatment was applied before the half-cell measurement. Each sample electrode was charged at a constant current density of 100 mA g^{-1} for 5 h and then discharged at a current density of 100 mA g^{-1} followed by two pulls at 25 and 8 mA g^{-1}. The obtained full capacities (8 mA g^{-1}) from the first thirteen cycles for the as-cast and annealed series are plotted in Fig. 5a and b, respectively. Most of the as-cast alloys (AB3.4-AB3.7) require one activation cycle to reach the maximum full capacity. The capacity degradation during cycling is caused by the combination of material disintegration and oxidation, which is less severe in the annealed samples. The high-rate (100 mA g^{-1}) and full capacities (8 mA g^{-1}) measured at the third cycle are listed in Table 5. Without using the metallic binder (Ni or Cu) in the electrode, the highest discharge current was set at 100 mA g^{-1} since the inter-particle connection will influence the resistance at rates higher than 100 mA g^{-1}. In both the as-cast and annealed series, AB3.5 and AB3.5A have the highest high-rate and full capacities. Both capacities increase with annealing in all five samples. The theoretical discharge capacity, based on the gaseous phase maximum hydrogen storage capacity as shown in Fig. 4 for each alloy is listed in the next column. While the as-cast samples with lower B/A ratios (3.3, 3.4, and 3.5) showed slightly higher full discharge capacities compared to their theoretical values, other samples showed 2–6% decreases comparing the same. It may be related to the incompletion of gaseous phase hydride formation in these as-cast samples with lower B/A ratios which exhibited relatively lower PCT slope factors (more tilted).

The activation behavior of the half-cell HRD, defined as the ratio of discharge capacity measured at 100 mA g^{-1} to that measured at 8 mA g^{-1}, for the first thirteen cycles for the as-cast and annealed samples are plotted in Fig. 6a and b, respectively. As seen in Table 5, at least two and three cycles are required for the HRD to stabilize in the as-cast and annealed series, respectively. The activation of the Nd-A_2B_7 is faster than those from AB_5 [64] and AB_2 [67] MH alloys. Annealing slows down the activation due to the reduction/elimination of some secondary phases which can be advantageous. The HRD values calculated from the capacities obtained at the third

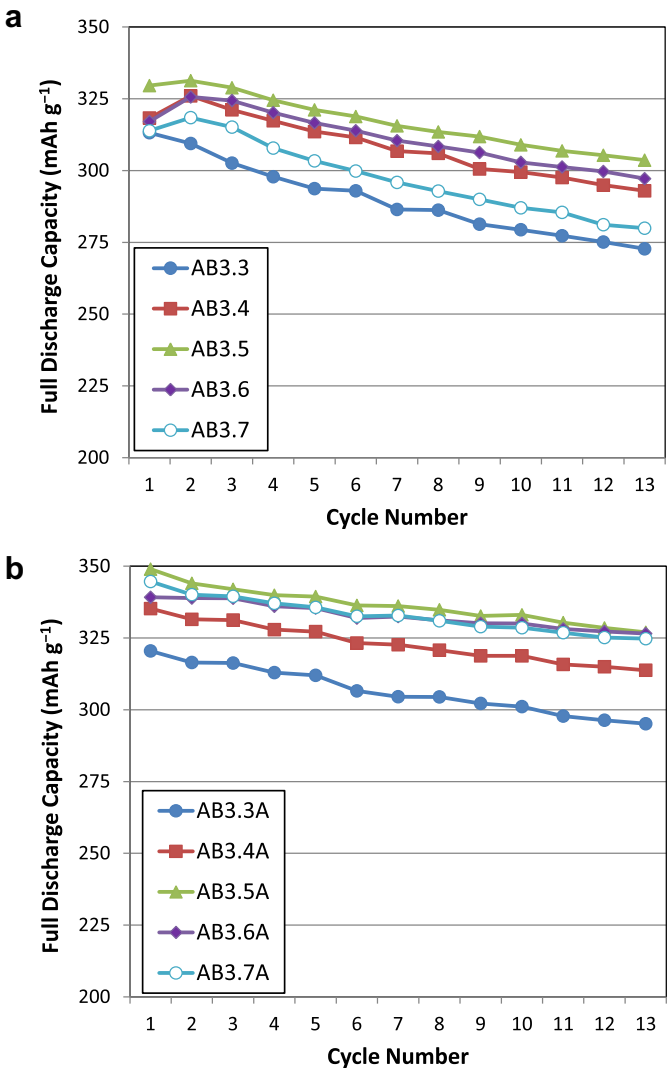

Fig. 5. Activation characteristic of half-cell discharge capacities measured at 8 mA g^{-1} for as-cast (a) and annealed (b) samples.

Table 5
Summary of electrochemical properties of un-annealed and annealed alloys.

Alloy	Full capacity @ 3rd cycle (mAh g^{-1})	High-rate capacity @ 3rd cycle (mAh g^{-1})	Theoretical capacity based on PCT (mAh g^{-1})	Activation cycle reaching 98% of stabilized HRD	HRD @ 3rd cycle	Diffusion coefficient D (10^{-10} cm^2 s^{-1})	Exchange current I_o (mA g^{-1})
AB3.3	302	291	297	2	0.96	6.6	35.9
AB3.4	321	310	295	2	0.97	5.5	23.6
AB3.5	329	321	322	2	0.98	6.0	22.3
AB3.6	324	317	330	2	0.98	6.2	25.4
AB3.7	315	307	324	1	0.98	5.9	17.2
AB3.3A	316	299	327	3	0.95	10.6	44.8
AB3.4A	331	317	348	3	0.96	6.2	64.9
AB3.5A	342	332	359	2	0.97	6.4	52.5
AB3.6A	339	328	359	3	0.97	4.5	48.5
AB3.7A	340	331	359	2	0.98	4.2	33.5

cycle are listed in Table 5. As the B/A ratio together with the Ni-content increase, the HRD value increases in both the as-cast and annealed series. By comparing HRD in Table 5, annealing is found to decrease the HRD value slightly for the same reason as in activation behavior change.

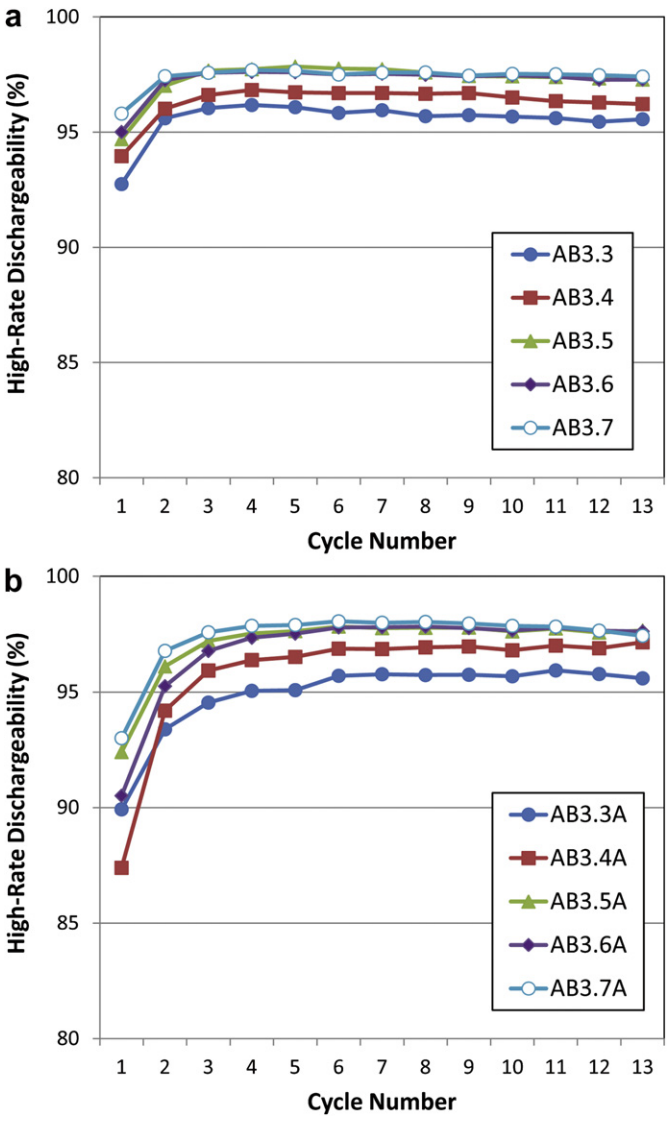

Fig. 6. Activation characteristic of high-rate dischargeability (ratio between capacities measured at 100 and 8 mA g^{-1}) for as-cast (a) and annealed (b) samples.

Conventionally, both the bulk diffusion coefficient (D) and surface exchange current (I_o) were used to study the source of HRD changes [65,69–73]. The details of both parameters' measurements were reported previously [38], and the values are listed in Table 5. All D values are higher than those in commercial available AB_2 ($D = 9.7 \times 10^{-11}$ cm^2 s^{-1}) and AB_5 MH alloys ($D = 2.55 \times 10^{-10}$ cm^2 s^{-1}) [72] and indicate easier hydrogen transportation in the bulk of Nd_2Ni_7-type of alloys, disregard the B/A ratio. In general, while the I_os of the as-cast samples are lower than those from commercial available AB_2 ($I_o = 32.1$ mA g^{-1}) and AB_5 (43.2 mA g^{-1}) [72], those from the annealed samples are higher than I_os from AB_2 and AB_5. This finding suggests the replacement in the MH alloy in the current Ni/MH battery with the annealed A_2B_7 alloys. In the as-cast series, while the D values are about the same, the I_o value decreases as the B/A ratio increases. In the annealed series, the D value decreases and the I_o value first increases and then decreases. In both cases, the increase in HRD value cannot be explained by either the bulk or surface property and may be related to the complicated multi-phase nature of these alloys which require further studies. Comparing both values before and after annealing reveal the following facts: while the bulk diffusion remains about the same except for AB3.3, the surface exchange current increases after annealing and thus contributes positively to the HRD performance.

4. Summary

Both the influences from stoichiometry and annealing on the structure, gaseous phase hydrogen storage, and electrochemical properties were studied for the Nd_2Ni_7-based multi-phase (including secondary phases such as $MgNdNi_4$, $NdNi_5$, $NdNi_3$, NdNi, Nd, and $CeNi_3$) alloys and summarized as follows:

With the increase in B/A ratio,

- the unit cell volume and abundance of the Nd_2Ni_7 main phase reduced while the abundances of the main secondary $NdNi_5$ and $MgNdNi_4$ phases increased, and those of NdNi and $CeNi_3$ phase decrease for both the as-cast and annealed series;
- the stoichiometry of the main Nd_2Ni_7 phase decreased in the as-cast series and remained constant at 3.3 for the annealed series;
- the maximum gaseous phase storage capacity first increased and then stabilized after B/A ratio in the main phase reached 3.3 while the reversible gaseous phase storage capacity increased in both the as-cast and annealed series;
- the equilibrium plateau pressure in the as-cast series decreased first and then increased while that in the annealed series increased;

- the heat of hydride formation (or the change in enthalpy) decreased in the as-cast series and remained about the same at −40 kJ mol^{-1} H_2 for the annealed series;
- both the full and high-rate electrochemical capacities increased and then decreased while the ratio (HRD) increased in both the as-cast and annealed series;
- the activation became easier; and
- the bulk diffusion of the annealed series decreased while the surface exchange current of the as-cast series decreased.

After annealing at 900 °C for 5 h,

- the lattice constants c/a ratio reduced;
- the unit cell volume of the main Nd_2Ni_7 phase decreased and its abundance increased;
- the abundances of all secondary phases reduced;
- the stoichiometry of the main Nd_2Ni_7 phase became 3.3;
- both the gaseous phase hydrogen storage and electrochemical capacity increased;
- HRD decreased slightly;
- the activation became more difficult;
- the bulk diffusion remained about the same for most of the alloys; and
- the surface exchange current increased.

Different from the conventional misch-metal based AB_5 MH alloy, the Nd-based (Nd, Mg)(Ni, Al)$_{3.5}$ alloy remained multiple-phase after annealing treatment, which makes the identification of the source of improvement in the electrochemical properties more difficult. In the future, the gaseous phase storage and electrochemical properties of each constituent phase and its synergetic effect to the main Nd_2Ni_7 phase should be fully investigated in order to further improve this series of alloys for Ni/MH application.

References

[1] Y. Liu, Y. Cao, L. Huang, M. Gao, H. Pan, J. Alloys Compd. 509 (2011) 675.
[2] A.V. Virkar, A. Raman, J. Less-Comm. Met. 18 (1969) 59.
[3] E. Parthé, R. Lemaire, Acta Crystallogr. Sect. B: Struct. Crystallogr. Cryst. Chem. 31 (1975) 879.
[4] K. Kadir, T. Sakai, I. Uehara, J. Alloys Compd. 257 (1997) 115.
[5] A. Férey, F. Cuevas, M. Latroche, B. Knosp, P. Bernard, Electrochim. Acta 54 (2009) 1710.
[6] T. Yamamoto, H. Inui, M. Yamaguchi, K. Sato, S. Fujitani, I. Yonezu, et al., Acta Mater. 45 (1997) 5213.
[7] Y. Nakamura, J. Nakamura, K. Iwase, E. Akiba, Nucl. Instrum. Methods Phys. Res. Sect. A 600 (2008) 297.
[8] J. Han, Z. Jiang, S. Jiao, Adv. Mater. Res. 156-157 (2010) 108.
[9] Z. Di, T. Yamamoto, H. Inui, M. Yamaguchi, Intermetallics 8 (2000) 391.
[10] Q. Zhang, M. Fang, T. Si, F. Fang, D. Sun, L. Ouyang, et al., J. Phys. Chem. C 114 (2010) 11686.
[11] K. Iwase, J. Sakaki, J. Matsuda, Y. Nakamura, T. Ishigaki, E. Akiba, Inorg. Chem. 50 (2011) 4548.
[12] L. Lemort, M. Latroche, B. Knosp, P. Bernard, J. Alloys Compd. 509 (2011) S823826.
[13] Z.Y. Liu, X.L. Yan, N. Wang, Y.J. Chai, D.L. Hou, Int. J. Hydrogen Energy 36 (2011) 4370.
[14] K. Kadir, N. Kuriyama, T. Sakai, I. Uehara, I. Eriksson, J. Alloys Compd. 284 (1999) 145.
[15] H. Pan, Y. Liu, M. Gao, Y. Zhu, Y. Lei, Q. Wang, J. Alloys Compd. 351 (2003) 228.
[16] Y. Liu, H. Pan, M. Gao, Y. Zhu, Y. Lei, Q. Wang, Electrochim. Acta 49 (2004) 545.
[17] H. Pan, Y. Liu, M. Gao, Y. Zhu, Y. Lei, Q. Wang, J. Electrochem, Soc. 151 (2004) A374.
[18] Y. Liu, H. Pan, M. Gao, R. Li, Y. Lei, J. Alloys Compd. 376 (2004) 296.
[19] H. Pan, R. Li, M. Gao, Y. Liu, Y. Lei, Q. Wang, Int. J. Hydrogen Energy 31 (2006) 1188.
[20] Y. Liu, H. Pan, M. Gao, H. Miao, Y. Lei, Q. Wang, Int. J. Hydrogen Energy 33 (2008) 124.
[21] Y. Zhang, X. Dong, D. Zhao, S. Guo, Y. Qi, X. Wang, Trans. Nonferrous Met. Soc. China 18 (2008) 857.
[22] Y. Chai, K. Asano, K. Sakaki, H. Enoki, E. Akiba, J. Alloys Compd. 485 (2009) 174.
[23] Y. Zhao, M. Gao, Y. Liu, L. Huang, H. Pan, J. Alloys Compd. 496 (2010) 454.
[24] S. Yasuoka, Y. Magari, T. Murata, T. Tanaka, J. Ishida, Nakamura, et al., J. Power Sources 156 (2006) 662.
[25] R. Tang, Y. Liu, C. Zhu, J. Zhu, G. Yu, Mater. Chem. Phys. 95 (2006) 130.
[26] R. Tang, Y. Liu, C. Zhu, J. Zhu, G. Yu, Intermetallics 14 (2006) 361.
[27] W. Xiong, H. Yan, F. Kong, B. Li, J. Li, Y. Zhang, Met. Funct. Mater. 15 (2008) 5.
[28] S. Ma, M. Gao, R. Li, H. Pan, Y. Lei, J. Alloys Compd. 457 (2008) 457.
[29] L. Liu, R. Tang, Y. Liu, Chin. J. Nonferrous Met. 13 (2003) 871.
[30] Z. Zhou, Y. Song, S. Cui, C. Lin, X. Qu, Chin. J. Nonferrous Met. 17 (2007) 45.
[31] Y. Luo, Q. Jia, T. Wu, L. Kang, J. Lanzhou Univ. Technol. 35 (2009) 1.
[32] Y. Li, S. Han, J. Li, X. Zhu, L. Hu, J. Alloys Compd. 458 (2008) 357.
[33] C. Pan, B. Yang, J. Iqbal, R. Yu, Rare Met., Mater. Eng. 367 (2011) 367.
[34] C.C. Pan, R. Yu International Symposium on Materials Issues in a Hydrogen Economy; 2007 Nov 12–15; Richmond, Virginia, USA, in: P. Jena, A. Kandalam, Q. Sun (Eds.), Materials Issues in a Hydrogen Economy, World Scientific Publishing Co, Singapore, 2009, p. 203.
[35] C. Pan, S. Yang, R. Yu, J. Shi, Y. Nakamura, J. Rare Earths 28 (2010) 286.
[36] C. Pan, W. Cai, J. Iqbal, Z. Wang, C. Geng, R. Yu, J. Rare Earths 28 (2010) 100.
[37] G.Y. Shang, S.M. Han, J.S. Hao, Y. Liu, X.L. Zhu, Y. Li, et al., J. Alloys Compd. 493 (2010) 573.
[38] F. Li, K. Young, T. Ouchi, M.A. Fetcenko, J. Alloys Compd. 471 (2009) 371.
[39] M.A. Fetcenko, K. Young, S.R. Ovshinsky, T. Ouchi, United States patent US 7393500. 2008.
[40] Z. Wang, X. Li, Q. Chen, H. Guo, W. Peng, B. Guo, J. Rare Earths 19 (2001) 29.
[41] O.L. Makarova, I.N. Goncharenko, F. Bourée, Phys. Rev. B: Conden. Matter Mater. Phys. 67 (2003) 134418–134421.
[42] P. Fisher, W. Hälg, L. Schlapbach, Th. von Wadkirch, Helv. Phys. Acta 51 (1978) 4.
[43] K. Young, T. Ouchi, M.A. Fetcenko, J. Alloys Compd. 480 (2009) 428.
[44] Y. Osumi, H. Suzuki, A. Kato, K. Oguro, S. Kawai, M. Kaneko, J. Less-Comm. Met. 89 (1983) 287.
[45] V.A. Yartys, A.B. Riabiv, R.V. Denys, M. Sato, R.G. Delaplane, J. Alloys Compd. 408-412 (2006) 273.
[46] Y.E. Filinchuk, K. Yvon, J. Alloys Compd. 446-447 (2007) 3.
[47] H. Nakano, S. Wakao, T. Shimizu, J. Alloys Compd. 253-254 (1997) 609.
[48] L. Guénée, V. Favre-Nicolin, K. Yvon, J. Alloys Compd. 348 (2003) 129.
[49] Z.M. Wang, H.Y. Zhou, G. Cheng, Z.F. Gu, A.B. Yu, J. Alloys Compd. 384 (2004) 279.
[50] X. Xu, H.Y. Zhou, R.P. Zou, S.L. Zhang, Z.M. Wang, J. Alloys Compd. 396 (2005) 247.
[51] S. Zhang, H. Zhou, Z. Wang, R.P. Zou, H. Xu, J. Alloys Compd. 398 (2005) 269.
[52] S. Zhang, Y. Zhao, H. Zhou, J. Mater. Process Technol. 174 (2006) 167.
[53] S. Zhang, Y. Zhao, G. Chen, X. Cheng, H. Sun, Mater. Process Technol. 198 (2008) 270.
[54] Y. Takaguchi, K. Tanaka, J. Alloys Compd. 297 (2000) 73.
[55] A. Drašner, Z. Blažina, J. Alloys Compd. 381 (2004) 188.
[56] H. Senoh, N. Kuriyama, Res. Chem. Intermed. 32 (2006) 431.
[57] K. Young, T. Ouchi, B. Huang, B. Chao, M.A. Fetcenko, L.A. Bendersky, et al., J. Alloys Compd. 506 (2010) 841.
[58] K. Young, J. Nei, T. Ouchi, M.A. Fetcenko, J. Alloys Compd. 509 (2011) 2277.
[59] H. Okamoto, J. Phase Equilib. Diffus. 27 (2006) 552.
[60] K. Young, T. Ouchi, J. Koch, M.A. Fetcenko, J. Alloys Compd. 477 (2009) 749.
[61] K. Young, R. Regmi, G. Lawes, T. Ouchi, B. Reichman, M.A. Fetcenko, J. Alloys Compd. 490 (2010) 282.
[62] Q. Zheng, Y. Chen, J. Wang, M. Tao, D. Tang, M. Tu, Trans. Nonferrous Met. Soc. China 14 (2004) 1129.
[63] Y. Osumi, Suiso-kyuzo-goukin No Syurui to Sono. New ed., . Agune Technology Center, Tokyo, Japan, 1999, p. 218.
[64] K. Young, T. Ouchi, B. Reichman, J. Koch, M.A. Fetcenko, J. Alloy Compd. 509 (2011) 7611.
[65] K. Young, T. Ouchi, B. Huang, B. Reichman, M.A. Fetcenko, Int. J. Hydrogen Energy 36 (2011) 12296.
[66] L. Schlapbach, A. Züttle, Nature 414 (2001) 353.
[67] K. Young, T. Ouchi, B. Huang, B. Reichman, M.A. Fetcenko, J. Power Sources 204 (2012) 205.
[68] K. young, T. Ouchi, J. Koch, M.A. Fetcenko, J. Alloys Compd. 510 (2012) 97.
[69] H. Pan, J. Ma, C. Wang, S. Chen, X. Wang, C. Chen, et al., J. Alloys Compd. 293-295 (1999) 648.
[70] R. Li, H. Pan, M. Gao, H. Miao, Y. Lei, J. Alloys Compd. 432 (2007) 183.
[71] K. Young, T. Ouchi, B. Huang, B. Reichman, M.A. Fetcenko, J. Power Sources 196 (2011) 8815.
[72] K. Young, B. Huang, R.K. Regmi, G. Lawes, Y. Liu, J. Alloys Compd. 506 (2010) 831.
[73] K. Young, M. Young, T. Ouchi, B. Reichman, M.A. Fetcenko, submitted to J. Power Sources